Influence of the Drying Temperature on the Performance and Binder Distribution of Sulfurized Poly(acrylonitrile) Cathodes

Influence of the Drying Temperature on the Performance and Binder Distribution of Sulfurized Poly(acrylonitrile) Cathodes

Journal:	*Journal of The Electrochemical Society*
Manuscript ID	JES-103999.R2
Manuscript Type:	Research Paper
Date Submitted by the Author:	15-Apr-2021
Complete List of Authors:	Niesen, Stefan; Mercedes-Benz AG Kappler, Julian; University of Stuttgart, Polymer Chemistry Trueck, Janina; Mercedes-Benz AG Veith, Lothar; Max Planck Institute for Polymer Research Weil, Tanja; Max Planck Institute for Polymer Research Soczka-Guth, Thomas; Mercedes-Benz AG Buchmeiser, Michael; University of Stuttgart, Polymer Chemistry
Keywords:	lithium-sulfur battery, sulfurized poly(acrylonitrile), SPAN, binder migration, ToF SIMS

Influence of the Drying Temperature on the Performance and Binder Distribution of Sulfurized Poly(acrylonitrile) Cathodes

Stefan Niesen,[1,2] Julian Kappler,[1] Janina Trück,[1,2] Lothar Veith,[3,*] Tanja Weil,[3] Thomas Soczka-Guth,[2] and Michael R. Buchmeiser[1,4,z]

[1]Institute of Polymer Chemistry, University of Stuttgart, 70569 Stuttgart, Germany

[2]Mercedes-Benz AG, RD/EBZ, 70327 Stuttgart, Germany

[3]Max Planck Institute for Polymer Research, 55128 Mainz, Germany

[4]German Institutes of Textile and Fiber Research (DITF) Denkendorf, 73770 Denkendorf, Germany

*Electrochemical Society Member.

[z]E-mail: michael.buchmeiser@ipoc.uni-stuttgart.de

Abstract

The drying of electrodes during the manufacturing process strongly affects both the cell performance and production costs of lithium-sulfur (Li-S) batteries. Herein, we present a detailed study on the effect of temperature during the drying process on the performance and binder distribution of sulfurized poly(acrylonitrile) (SPAN) based electrodes using poly(vinylidene fluoride) (PVdF) or poly(acrylic acid) (PAA) as the binder. The electrochemical performance of the PVdF- and PAA-based cathode coatings, which were dried at three different temperatures (30 °C, 60 °C and 90 °C), is analyzed by cycling against lithium metal and utilizing reference-assisted impedance spectroscopy. Time-of-flight secondary ion mass spectrometry (ToF SIMS) is applied on both the surface and the cross-section of the electrodes to determine the binder distribution. Contrary to the PAA-based cathodes, PVdF based electrodes exhibit binder migration to the electrode surface at elevated coating drying temperatures. The enrichment of PVdF on the surface leads to an increase in the charge transfer resistance and thereby reduces the rate capability.

Introduction

Since several countries passed legislation to lower carbon dioxide (CO_2) emissions in the transport sector, many car manufacturers have committed themselves to electrifying their fleets. Therefore, the demand for energy storage devices will rise substantially in the near future and the search for novel high-performance battery materials will intensify.[1-3] Besides state of the art lithium-ion (Li-ion) battery technology, several promising post-Li-ion technologies have emerged.[4, 5] Among these, lithium-sulfur (Li-S) batteries are of particular interest as they exhibit a high theoretical capacity of 1675 mAh g_S^{-1} and consists of mostly abundant and low-cost raw materials.[6-8]

However, any large-scale commercialization of Li-S battery technology has not yet been achieved, mainly due to the insulating nature of sulfur and the dissolution of polysulfides during operation, which results in a harmful internal polysulfide shuttle.[9-13] Owing to the absence of a polysulfide shuttle, high intrinsic electrical conductivity, excellent cycling stability and compatibility with carbonate-based electrolytes, sulfurized poly(acrylonitrile) (SPAN) is a promising cathode material for Li-S batteries and thereby a desirable technology for future energy storage applications.[14-20]

Nevertheless, prior to any large-scale production of SPAN-based electrodes, several parameters need to be addressed.[21, 22] One of these parameters is the drying temperature of the electrode coating. To decrease costs and overall production time, a higher electrode drying temperature is favorable.[23, 24] In the field of Li-ion batteries, a detrimental effect of an increase in the drying temperature on the rate capability is known for poly(vinylidene fluoride) (PVdF) based graphite electrodes. These differences in rate capability are caused by an uneven binder distribution, which results in an additional resistance at the surface of the electrodes.[25-27] Furthermore, a negative effect of an inhomogeneous binder distribution on the adhesion force, caused by an increased coating drying temperature, was observed for graphite anodes.[28, 29]

In general, the binder strongly influences the obtainable rate capability and cycling stability especially within post-Li-ion batteries and should therefore be prudently chosen.[30-32] Besides PVdF, poly(acrylic acid) (PAA) is a commonly used binder for SPAN-based cathodes.[14] Contrary to PVdF, PAA has functional groups which can interact with the electrode materials and the current collector.[33] Therefore, PVdF- and PAA-based SPAN cathodes can be expected

to exhibit different coating drying behavior.

Until now, the drying process of SPAN electrode coatings was an insufficiently understood processing step during the manufacturing of Li-SPAN cells. Here, the impact of the drying temperature on the electrochemical performance was verified by cycling both PAA-and PVdF-based SPAN electrode coatings, dried at three different temperatures (30 °C, 60 °C and 90 °C), against lithium metal. Additionally, differences in the internal resistances within the obtained electrodes were identified by using reference-assisted electrochemical impedance spectroscopy (EIS). Subsequently, the binder distribution of the obtained coatings was analyzed by time-of-flight secondary ion mass spectrometry (ToF-SIMS).

Experimental

Synthesis of Sulfurized Poly(acrylonitrile) (SPAN). For the synthesis of SPAN, poly(acrylonitrile) (PAN, M_n = 54,900 g/mol, $Đ$ = 4.4) was placed in a quartz glass tube and mixed with excess elemental sulfur (Carl Roth, Germany). The quartz glass tube was placed into a furnace (Nabertherm, Germany) and the following two-step temperature program was used. The sample was heated to 150 °C applying a heating rate of 300 °C h^{-1} and kept at this temperature for 30 min. Then the sample was heated to 550 °C within 2 h and held at this temperature for 5 h. During the entire heating process, a nitrogen flow (200 L h^{-1}) was applied. After cooling to room temperature, elemental sulfur was removed via extensive Soxhlet extraction with toluene at 150 °C for 24 h. The obtained SPAN particles were dried under vacuum overnight. All samples had a sulfur content of 38 ± 1 wt%.

Electrode Preparation and Drying. Electrode slurries were prepared by mixing the obtained SPAN particles (80 wt%), Super C65 conducting carbon (10 wt%, MTI Corporation, USA) and a polymeric binder (10 wt%). Poly(vinylidene fluoride) (PVdF, Kynar, Arkema, France) and poly(acrylic acid) (PAA, Sigma Aldrich, Germany), respectively, were used as binders. Prior to mixing, PVdF and PAA were dissolved in *N*-methyl-2-pyrrolidone (NMP, anhydrous, 99.5 %, Sigma-Aldrich). The SPAN:NMP ratio was set to 1:5 (w:w). After dissolving the binder, a defined amount of SPAN and C65 was added to the binder solution and mixed twice with a planetary mixer (Thinky, Japan) at 2000 rpm for 3 min. The resulting slurry was cast on a carbon-coated aluminum foil (t = 18 µm, MTI Corporation, USA) using a film coater

(Erichsen, Germany) adjusting a wet film thickness of 300 µm. The solvent was evaporated on a heated vacuum plate for 8 h at 30 °C, 60 °C or 90 °C. After drying on a heated vacuum plate, the electrodes were dried in a vacuum chamber at 60 °C for at least 2 h. The resulting areal capacity of the SPAN cathodes was 2.4 ± 0.2 mAh cm^{-2}.

Electrochemical Characterization. To verify the influence of the coating drying temperature on the rate capability of the SPAN cathodes, coin cells (CR2032, Hohsen Corporation, Japan) were assembled in an argon-filled glovebox (H_2O and O_2 concentration ≤ 0.1 ppm, MBraun, Germany) by sandwiching two layers of glass fiber separator (Ø = 16 mm, Whatman, UK) between a SPAN electrode (Ø = 12 mm) and a lithium metal anode (Ø = 14 mm, Alfa Aesar, USA). 130 µL of a commercially available electrolyte (1 M $LiPF_6$ in EC:DEC (1:1, v:v)), Sigma Aldrich, Germany) with the addition of 10 wt% fluoroethylene carbonate (FEC, Sigma Aldrich, Germany) was used as the electrolyte.

Electrochemical testing was performed with the aid of a battery cycler (BasyTec, Germany) in a voltage range of 1.0 – 3.0 V vs. Li/Li^+. To investigate the rate capability, all cells were cycled galvanostatically at C-rates ranging from C/4 (~ 0.6 mA cm^{-2}) to 4C (~ 9.6 mA cm^{-2}). Each cycling experiment included a resting period of 2 h to ensure complete wetting of the separator. For the long-term cycling experiments, five preformation cycles at C/4 were applied. Specific capacity and current density were calculated based on the mass of sulfur in the cathode using a theoretical sulfur capacity of 1675 mAh g_S^{-1}.

Electrochemical impedance spectroscopy was measured in PAT-cells (EL-Cell, Germany). Cells were assembled in an argon-filled glove box by sandwiching two layers of glass fiber separator (Ø = 21.6 mm, Whatman, UK) between a SPAN electrode (Ø = 16 mm) and a lithium metal anode (Ø = 18 mm, Alfa Aesar, USA). In between the separators, a partially insulated stainless steel finger-shaped reference electrode (EL-Cell, Germany) was placed and lithiated by applying a current of 1 mA for 6 h versus the lithium metal anode. For impedance measurements, 200 µL of 1 M $LiPF_6$ in EC:DEC (1:1, v:v, Sigma Aldrich, Germany) with an additional 10 wt% fluoroethylene carbonate (FEC, Sigma Aldrich, Germany) were used as the electrolyte. Impedance spectra were recorded with a potentiostat (Biologic, France) at an open-circuit voltage (OCV) at a state-of-charge (SOC) of 50 % during charging in a frequency range

between 200 kHz and 50 mHz with a 10 mV voltage perturbation. Before impedance measurements, the cells were cycled for five preformation cycles at C/4. All cells were measured in a climate room at 24 °C.

Time-of-Flight Secondary Ion Mass Spectrometry (ToF-SIMS). Spectra were recorded on a TOF-SIMS 5 (ION-TOF GmbH, Germany) instrument using a 30 keV Bi_3^+ primary ion beam (current: 0.15 pA, cycle time: 150 µs, mass range 1-2070 Da) with raster scanning areas of 200 × 200 µm^2. Images were acquired using a 30 keV Bi_3^+ primary ion beam (current: 0.05 pA, cycle time: 100 µs, mass range 1-920 Da) with raster scanning areas of 150 × 150 µm^2. Mass calibration of the data sets was performed using the signals of C^-, CH^-, C_2H^-, C_4H^- and C_6H^- in the negative ion polarity and of CH_3^+, $C_2H_3^+$, $C_3H_5^+$ and $C_4H_7^+$ in the positive ion polarity.

Results and Discussion

To assess the significance of the drying process on the rate capability of PAA- and PVdF-based SPAN cathodes, the obtained electrodes were cycled at alternating rates against lithium metal. Figure 1 illustrates the discharge capacities of the PVdF- and PAA-based SPAN electrodes, dried at three different temperatures (30 °C, 60 °C and 90 °C), at various C-rates (C/4 – 4C). For the PVdF-based cathodes, the discharge capacities decreased with increasing coating drying temperature at C-rates higher than C/2. At 4 C, the obtainable capacity was 544 mAh g_S^{-1}, 367 mAh g_S^{-1} and 237 mAh g_S^{-1} for the PVdF coatings dried at 30 °C, 60 °C and 90 °C, respectively. At lower rates (≤ C/2), no effect of the drying temperature on the performance of the PVdF-based cathodes was observed. The capacity of the cells at C/4 and C/2 before cycling at higher rates was identical to the capacity after cycling at higher rates. Therefore, the capacity drop at higher rates is reversible and not caused by cell degradation. In contrast to the electrodes prepared with PVdF, the coating drying temperature had no impact on the rate capability of the PAA-based electrodes. Interestingly, the rate capability of the PVdF-based cathodes dried at 30 °C, was almost identical to the rate capability of the PAA-based cathodes, which implies that the low rate capability of the PVdF-based electrodes is caused solely by an increased drying temperature (> 30 °C) and not by the nature of the binder itself. Figure 2 shows the voltage profiles of the tested electrodes, which were extracted

from the third 4C cycle of the rate capability tests. With increasing coating temperature the voltage profiles of the PVdF-based electrodes are shifted to lower voltages during discharge and higher voltages during the charging of the cell. For the cathodes prepared with PAA, no shift in the voltage profiles was observed. Consequently, the loss of capacity at higher rates of the PVdF-based coatings originates from incomplete discharge or charge of the cells, caused by an increase in overpotential at elevated coating drying temperatures.

To verify the influence of the drying process on the internal resistance of the obtained PVdF- and PAA-based cathodes, reference-assisted impedance measurements were conducted. Impedance measurements with a reference electrode in a three-electrode cell configuration allows the disentangling of the impedance signal of the anode and cathode.[34] Here, a lithiated finger-shaped stainless steel reference electrode, which was placed in the geometrical middle between anode and cathode instead of the outer edge of the cell stack, was applied. By placing the reference electrode at the center of the cell, the impedance of the cathode can be measured without artifacts caused by electric field inhomogeneity.[35] The reference electrode was lithiated by applying a small current versus the lithium metal anode. After cycling for five preformation cycles at C/4, the impedance of the cells was measured at an SOC of 50 % during the charging step. Figure 3 shows the Nyquist plots of the PVdF- and PAA-based SPAN electrode coatings, which were dried at different coating temperatures. The obtained plots were fitted with the equivalent circuit model (Figure S1, Supporting Information), consisting of a high frequency resistance (R_1), two R/Q elements (R_2/Q_1, R_3/Q_2) and a Warburg element (W_1) in series. The two R/Q elements were assigned to the contact resistance between coating and current collector (R_2/Q_1) and the charge transfer resistance (R_3/Q_2). The Warburg element was applied to model Li^+ diffusion. The exact fitted data is given in Table S1 (Supporting Information). Since the contact resistance (R_2) was almost identical for all measurements (~ 2 Ω), the following discussion will solely focus on distinctions in the charge transfer resistance (R_3) and differences in the high-frequency region. In the case of PVdF-based cathodes, the charge transfer resistance raised sharply with increasing coating drying temperature and was 5 Ω, 10 Ω and 14 Ω applying a coating drying temperature of 30 °C, 60 °C and 90 °C, respectively. Additionally, by comparing the angles of the high frequency branch e.g., PVdF-30°C vs. PVdF-90°C, a

coating drying temperature-induced increase in the slope of the Warburg diffusion element was observed. Contrary to the PVdF-based cathodes, the charge transfer resistances of the PAA-based cathodes remained almost constant (3 Ω - 4 Ω) and no change in the angle of the high frequency region was observed within the investigated coating drying temperature range. The obtained impedance results indicate that the detrimental effect of the drying process on the rate capability of the PVdF-based electrodes is caused by an increase in the charge transfer resistance and a more pronounced Li^+ diffusion limitation with increasing coating drying temperature.

In order to assess whether the coating drying temperature has an additional harmful effect on the cycle life of the PVdF-based cathodes, the capacity retention was evaluated by cycling the PVdF-based electrodes vs. lithium metal at 1C for 500 cycles. The results of the long-term cycling tests are illustrated in Figure S2 (Supporting Information). No impact of the temperature during the drying process on the capacity retention of the PVdF-based cathodes was observed, indicating that the drying temperature solely affects the rate capability.

To verify whether the observed distinctions in the rate capabilities, charge transfer resistances and Li^+ diffusion were caused by an inhomogeneous binder distribution, ToF-SIMS measurements were applied to analyze the binder distribution within the pristine PAA- and PVdF-based cathodes. ToF-SIMS is a powerful tool to provide fragment-specific information of surfaces.[36-38] Notably, to the best of our knowledge, this is the first time ToF-SIMS was used to elucidate the binder distribution within a battery electrode. First, ToF-SIMS measurements were carried out on the surface of the electrodes. Figure 4 illustrates the ToF-SIMS images of the surfaces of the PVdF- and PAA-based electrode coatings. The detected fragments on the electrode surfaces include the diagnostic ions CN^- (red), C_2^- (green), F^- (blue) and C_2HO^- (blue) for SPAN, C65 Carbon, PVdF and PAA, respectively. The signal intensity scales were adjusted to enable a comparison between the different drying temperatures. Reference ToF-SIMS spectra of the pure electrode materials are depicted in Figures S3-S5 (Supporting Information).

As can be seen in Figures 4a-c, the F^- signal intensity (shown in blue) on the surface of the PVdF-based electrode increased sharply with increasing coating drying temperatures, suggesting a larger amount of PVdF on the surface. Especially at higher drying temperatures

(> 30 °C) high PVdF signal intensities, which cover almost the entire electrode surface, were obtained. For the PAA-based electrode coatings, only a minor influence of the drying temperature on the PAA intensities on the surface of the electrodes was observed (Figure 4d-f). Contrary to the PVdF-based cathodes, even at the highest drying temperature (90 °C) no complete coverage of the surface by a distinct binder layer was observed for the PAA-based electrode surface. This suggests that the recognized harmful influence of the coating drying temperature on the rate capability of the PVdF-based electrodes originates from the formation of a PVdF layer on the surface.

To get a more detailed understanding of the influence of the drying temperature on the binder distribution within the PVdF- and PAA-based electrode coatings, ToF-SIMS images of electrode cross-sections (created by cutting liquid N_2-frozen electrodes with scissors) were acquired. Detected fragments were F^- for PVdF (green) and $C_3H_3O_2^-$ (green) for PAA. The O^- and AlO^- fragments (red) were used as diagnostic ions for the current collector visible on top of the images. The detected signal distributions (F^- or $C_3H_3O_2^-$) matched the expected thickness (~ 90 µm, previously determined with a thickness gauge) of the electrodes. The PVdF-based cathodes dried at 30 °C showed a homogenous PVdF distribution based on the detected F^- signal (Figure 5a). At higher drying temperatures (60 °C and 90 °C), the PVdF binder became less homogenously distributed (Figure 5b-c). Several spots with notably high F^- intensities (bright green, exemplary spots marked with red circles) became visible in the coatings dried at elevated temperatures (> 30 °C), which indicates an agglomeration of the PVdF binder at drying temperatures higher than 30 °C. In particular, closer to the electrode surface (lower part of the images) several spots with increased F^- signal intensities became visible in the ToF-SIMS images of the PVdF-based electrode coatings dried at 60 °C and 90 °C. As can be seen by comparing Figures 4b and 4c, the extent of the PVdF agglomeration close to the electrode surface increases notably with elevating coating drying temperature. Therefore, it can be assumed that the detected PVdF agglomerates close to or at the electrode surface are formed by the migration of the PVdF binder during the drying process at elevated drying temperatures (i.e. higher solvent evaporation rates). Since PVdF is an insulator and exhibits only poor ionic conductivity, an agglomeration of PVdF (e.g. on the surface) could potentially increase the

electrical and/or ionic resistance of the electrode. Consequently, the obtained ToF-SIMS results strongly suggest that the detrimental effect of drying at elevated temperatures (> 30 °C) on the charge transfer resistance and Li^+ diffusion of PVdF-based electrodes, which led to a reduction in rate capability, is most likely caused by a migration of the PVdF binder to the electrode surface induced by higher solvent evaporation rates. Given that the ToF-SIMS measurements were repeated several times and that the described effect of the drying temperature on the PVdF distribution was visible in all measurements, the migration of PVdF is solely caused by the drying temperature and not by a deviation in the roughness of the electrodes. The observed influence of drying temperature on the rate capability and binder distribution of the SPAN cathodes prepared with PVdF is in good agreement with studies conducted on Li-ion anodes. Jaiser et al. and Morasch et al. investigated the effect of the drying temperature on the rate capability and binder distribution of PVdF-based graphite anodes.[25, 29] Both studies demonstrates that the harmful effect of an increase in the coating drying temperature on the rate capability originates from the enrichment of PVdF on the electrode surface.

In the ToF-SIMS images of the PAA-based electrode cross-sections, a mostly homogenous distribution of the C_2HO^- signal with similarly high intensity in the electrode area was observed for all the investigated drying temperatures (Figure 5d-f). Elevated $C_3H_3O_2^-$ intensities became visible close to the current collector in the images of the PAA-based coatings which were dried at 30 °C and 90 °C. Since the carbon-coated current collector exhibits oxygen functionalities, which can form hydrogen bonds, the increased signal intensity of the PAA-based signal ($C_3H_3O_2^-$) close to the current collector can potentially be explained by an interaction of the PAA binder with the carbon coating on the current collector.[39] Additionally, an increased ion collision-cascade efficiency on the metal current collector might also lead to elevated secondary ion intensities in its vicinity. Considering that no influence of the coating drying temperature on the rate capability and impedance was detected during the electrochemical characterization, the assumed PAA layer at the coating / current collector interface, which is visible in particular in Figures 5d, has no detrimental effect on the performance of the PAA-based cathodes and can therefore be disregarded.

The distinction in the migration behavior between PVdF- and PAA-based electrodes during

the drying process can potentially be explained by differences in the structures of the binders. In contrast to PAA, PVdF has no carboxylic acid groups which can interact via hydrogen bonds with the electrode materials (SPAN, conductive carbon) and / or current collector. It has previously been shown that the adhesion ability of binders to the electrode materials can have a strong impact on both electrode processing and performance. For example, Yoo et al. showed that the usage of hydroxyl-functionalized PVdF compared to non-functionalized PVdF as a binder for graphite anodes led to an enhanced adhesion between active material and binder and thereby to a more homogenous binder distribution.[40-42] Therefore, the inability of PVdF to form such strong interactions with the electrode materials likely promotes its mobility, which ultimately leads to a severe agglomeration and migration of PVdF towards the surface at elevated coating drying temperatures. The migration of PVdF to the surface is expected to be caused by phase separation between PVdF and other electrode materials, which itself is provoked by the more pronounced evaporation of NMP at higher drying temperatures. Besides the inability of PVdF to form sufficient adhesion with the electrode materials, a stronger interaction of PVdF and NMP (relative to PAA and NMP) could additionally be made accountable for the observed migration of PVdF. If the interaction between the binder and solvent is too strong, the binder may segregate to the surface during solvent evaporation at high drying rates. A detailed study on the migration mechanism of PVdF-based SPAN cathodes is ongoing.

Conclusions

The influence of the coating drying temperature on the electrochemical performance and binder distribution of PVdF- and PAA-based cathodes was investigated by utilizing reference-assisted impedance spectroscopy and ToF-SIMS. The rate capability of the PVdF-based electrodes decreased sharply with increasing coating drying temperature, whereas the rate capability of the PAA-based electrodes was independent of the temperature applied during the drying process. Impedance measurements of the PVdF-based cathodes revealed that the reduction in the rate capability was caused by an increase in the charge transfer resistance and a more pronounced Li^+ diffusion limitation. ToF-SIMS measurements showed that the harmful effect of an increase in the coating drying temperature on the charge transfer resistance and Li^+

diffusion of the PVdF-based electrodes originates from the enrichment of PVdF on the electrode surface.

Acknowledgments

We gratefully acknowledge funding and support from the German Federal Ministry for Economic Affairs and Energy (BMWi, project no. S50400, *FiMaLiS*). Dralon GmbH (Germany) is gratefully acknowledged for providing the PAN particles. Furthermore, the authors thank M. Siodlaczek, A. M. Fox, S. Murugan and J. V. Musso (Institute of Polymer Chemistry, University of Stuttgart) for fruitful discussions.

References

1. E. A. Olivetti, G. Ceder, G. G. Gaustad, and X. Fu, *Joule*, **1** 229-243 (2017).
2. H. Budde-Meiwes, J. Drillkens, B. Lunz, J. Muennix, S. Rothgang, J. Kowal, and D. U. Sauer, *Proc. Inst. Mech. Eng. D*, **227** 761-776 (2013).
3. N. Nitta, F. Wu, J. T. Lee, and G. Yushin, *Mater. Today*, **18** 252-264 (2015).
4. J. W. Choi and D. Aurbach, *Nat. Rev. Mater.*, **1** 1-16 (2016).
5. M. Walter, M. V. Kovalenko, and K. V. Kravchyk, *New J. Chem.*, **44** 1677-1683 (2020).
6. A. Manthiram, Y. Fu, S. H. Chung, C. Zu, and Y. S. Su, *Chem. Rev.*, **114** 11751-11787 (2014).
7. G. Benveniste, H. Rallo, L. Canals Casals, A. Merino, and B. Amante, *J. Environ. Manage.*, **226** 1-12 (2018).
8. Q. Pang, X. Liang, C. Y. Kwok, and L. F. Nazar, *Nat. Energy*, **1** 1-11 (2016).
9. P. T. Dirlam, R. S. Glass, K. Char, and J. Pyun, *J. Polym. Sci. A Polym. Chem.*, **55** 1635-1668 (2017).
10. V. S. Kolosnitsyn, E. V. Kuzmina, and E. V. Karaseva, *J. Power Sources*, **274** 203-210 (2015).
11. J. Scheers, S. Fantini, and P. Johansson, *J. Power Sources*, **255** 204-218 (2014).
12. R. Mukkabla and M. R. Buchmeiser, *J. Mater. Chem.*, **8** (11), 5379-5394 (2020).
13. T. Ould Ely, D. Kamzabek, D. Chakraborty, and M. F. Doherty, *ACS Appl. Energy*

Mater., **1** 1783-1814 (2018).

14. H. M. Kim, J. Y. Hwang, D. Aurbach, and Y. K. Sun, *J. Phys. Chem. Lett.*, **8** 5331-5337 (2017).
15. J. Fanous, M. Wegner, J. Grimminger, Ä. Andresen, and M. R. Buchmeiser, *Chem. Mater.*, **23** 5024-5028 (2011).
16. J. Fanous, M. Wegner, M. B. M. Spera, and M. R. Buchmeiser, *J. Electrochem. Soc.* , **160** A1169 (2013).
17. M. Frey, R. K. Zenn, S. Warneke, K. Müller, A. Hintennach, R. E. Dinnebier, and M. R. Buchmeiser, *ACS Energy Lett.*, **2** 595-604 (2017).
18. H. Yang, J. Chen, J. Yang, and J. Wang, *Angew. Chem. Int. Ed.*, **59** 7306-7318 (2020).
19. S. Warneke, A. Hintennach, and M. R. Buchmeiser, *J. Electrochem. Soc.* , **165** (2018).
20. T. Lebherz, M. Frey, A. Hintennach, and M. R. Buchmeiser, *RSC Advances*, **9** (13), 7181-7188 (2019).
21. O. Gröger, H. A. Gasteiger, and J.-P. Suchsland, *J. Electrochem. Soc.*, **162** A2605 (2015).
22. S. Dörfler, H. Althues, P. Härtel, T. Abendroth, B. Schumm, and S. Kaskel, *Joule*, **4** 539-554 (2020).
23. D. L. Wood, J. D. Quass, J. Li, S. Ahmed, D. Ventola, and C. Daniel, *Dry. Technol.*, **36** 234-244 (2017).
24. D. L. Wood, J. Li, and C. Daniel, *J. Power Sources*, **275** 234-242 (2015).
25. R. Morasch, Landesfeind J., Suthar B., Gasteiger H.A., *J. Electrochem. Soc.*, **165** A3459-A3467 (2018).
26. M. Müller, L. Pfaffmann, S. Jaiser, M. Baunach, V. Trouillet, F. Scheiba, P. Scharfer, W. Schabel, and W. Bauer, *J. Power Sources*, **340** 1-5 (2017).
27. B. G. Westphal and A. Kwade, *J. Energy Storage*, **18** 509-517 (2018).
28. J. Kumberg, M. Müller, R. Diehm, S. Spiegel, C. Wachsmann, W. Bauer, P. Scharfer, and W. Schabel, *Energy Technol.*, **7** (2019).
29. S. Jaiser, M. Müller, M. Baunach, W. Bauer, P. Scharfer, and W. Schabel, *J. Power*

Sources, **318** 210-219 (2016).

30. H. Yuan, J.-Q. Huang, H.-J. Peng, M.-M. Titirici, R. Xiang, R. Chen, Q. Liu, and Q. Zhang, *Adv. Energy Mater.* , **8** (31), 1802107 (2018).
31. K. K. Rajeev, E. Kim, J. Nam, S. Lee, J. Mun, and T.-H. Kim, *Electrochim. Acta*, **333** 135532 (2020).
32. S. Lim, R. L. Thankamony, T. Yim, H. Chu, Y. J. Kim, J. Mun, and T. H. Kim, *ACS Appl Mater Interfaces*, **7** (3), 1401-1405 (2015).
33. J.-T. Li, Z.-Y. Wu, Y.-Q. Lu, Y. Zhou, Q.-S. Huang, L. Huang, and S.-G. Sun, *Adv. Energy Mater.*, **7** (24), 1701185 (2017).
34. M. Dolle´, F. Orsini, A. Gozdz, S., and J.-M. Tarascon, *J. Electrochem. Soc.*, **148** A851 (2001).
35. Y. Hoshi, Y. Narita, K. Honda, T. Ohtaki, I. Shitanda, and M. Itagaki, *J. Power Sources*, **288** 168-175 (2015).
36. J.-H. Song, J.-T. Yeon, J.-Y. Jang, J.-G. Han, S.-M. Lee, and N.-S. Choi, *J. Electrochem. Soc.* , **160** A873 (2013).
37. E. M. Erickson, W. Li, A. Dolocan, and A. Manthiram, *ACS Appl. Mater. Interfaces*, **12** 16451-16461 (2020).
38. T. Sui, B. Song, J. Dluhos, L. Lu, and A. M. Korsunsky, *Nano Energy*, **17** 254-260 (2015).
39. M. Kuenzel, D. Bresser, G.-T. Kim, P. Axmann, M. Wohlfahrt-Mehrens, and S. Passerini, *ACS Appl. Energy Mater.*, **3** 218-230 (2019).
40. C.-C. Li and Y.-S. Lin, *J. Power Sources*, **220** 413-421 (2012).
41. Y.-W. W. Chia-Chen Li, *J. Electrochem. Soc.*, **158** A1361 (2011).
42. C. W. F. Mikyong Yoo, Shoichiro Mori, *Chem. Mater.*, **15** (850-861), (2003).

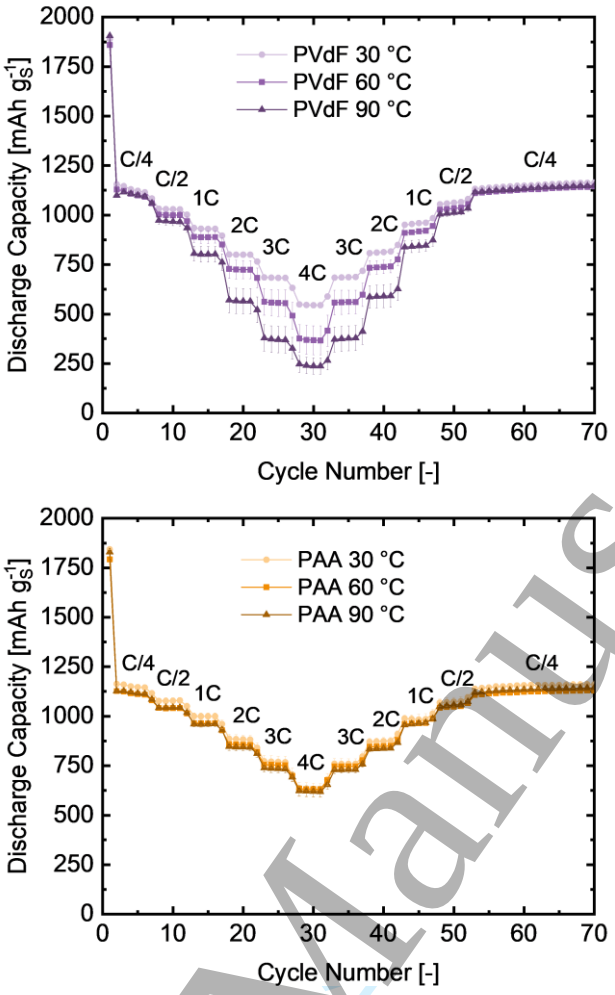

Figure 1: Galvanostatic cycling of PVdF- (upper panel) and PAA- (lower panel) based SPAN coatings dried at different temperatures (30 °C, 60 °C, 90 °C) vs. lithium metal between 1 - 3 V vs. Li/Li^+. Applied current range: C/4 (~ 0.6 mA cm^{-2}) to 4C (~ 9.6 mA cm^{-2}). The error bars represent the standard deviation of at least two independent measurements.

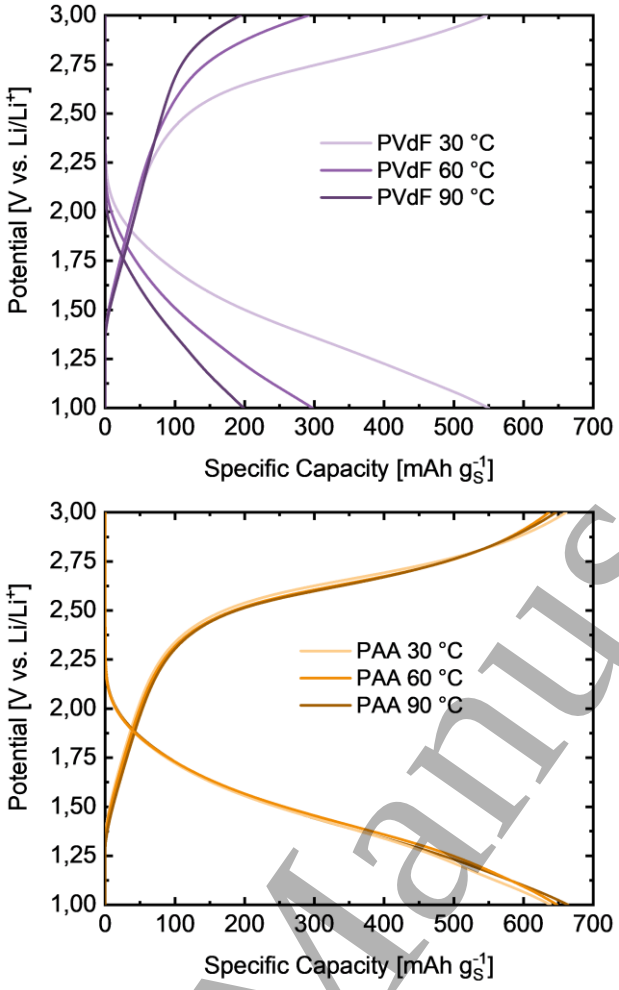

Figure 2: Voltage profiles of PVdF- (upper panel) and PAA- (lower panel) based SPAN coatings dried at different temperatures (30 °C, 60 °C, 90 °) at 4C extracted from the rate capability tests.

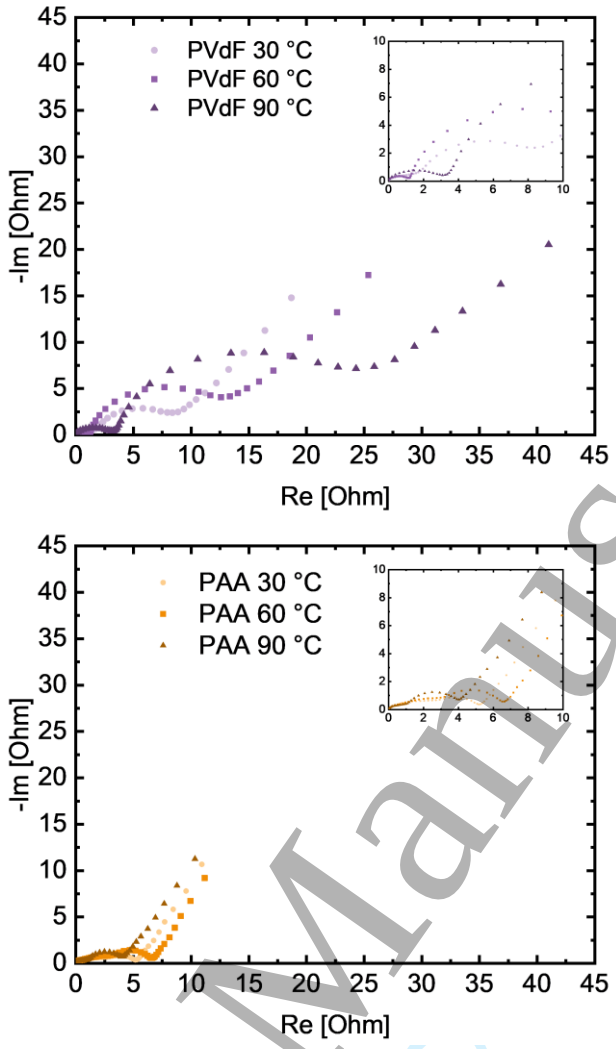

Figure 3: Nyquist plots of the SPAN cathodes with PVdF (upper panel) and PAA (lower panel) as binder dried at different coating drying temperatures (30 °C, 60 °C, 90 °C) measured in Li-SPAN cells utilizing the lithiated stainless steel finger-shaped reference electrode. For impedance measurements, cells were preformed for five cycles at C/4 (~ 0.6 mA cm^{-2}) and then charged to 50 % SOC. The impedance spectra were acquired at OCV between 200 kHz and 50 mHz with an amplitude of 10 mV. For better comparability, the high-frequency resistance (R_1) was subtracted from all the measurements.

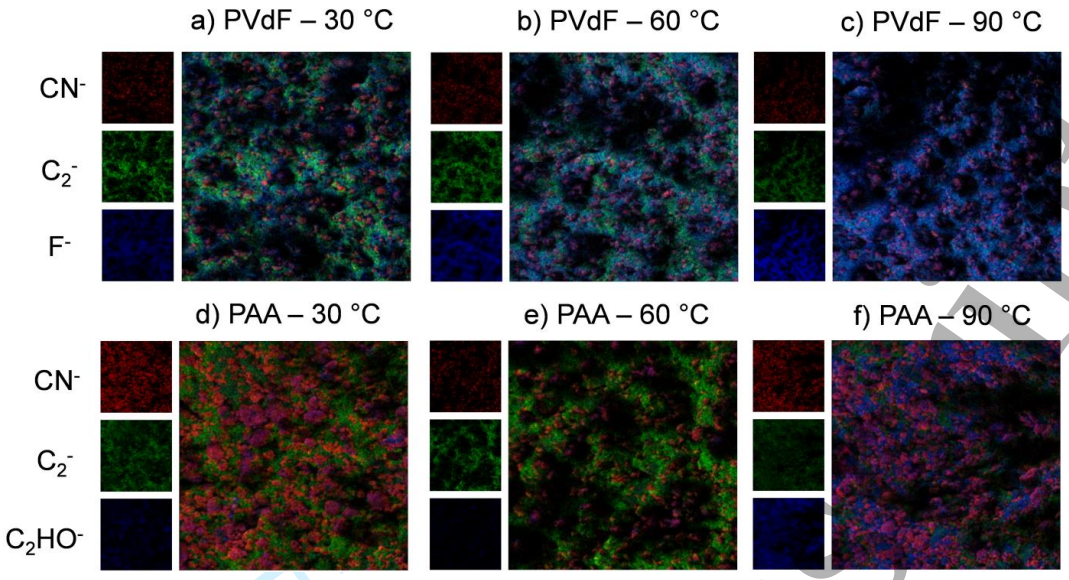

Figure 4: ToF-SIMS images of the electrode surfaces with intensity scales matched to enable for comparison within the binder type. Upper panel: pristine PVdF-based electrode coatings dried at 30 °C (a), 60 °C (b) and 90 °C (c). Lower panel: pristine PAA-based electrode coatings dried at 30 °C (d), 60 °C (e) and 90 °C (f). Detected fragments include CN^- (SPAN, red), C_2^- (C65 Carbon, green), F^- (PVdF, blue) and C_2HO^- (PAA, blue). The raster scanning area is 150 × 150 μm^2.

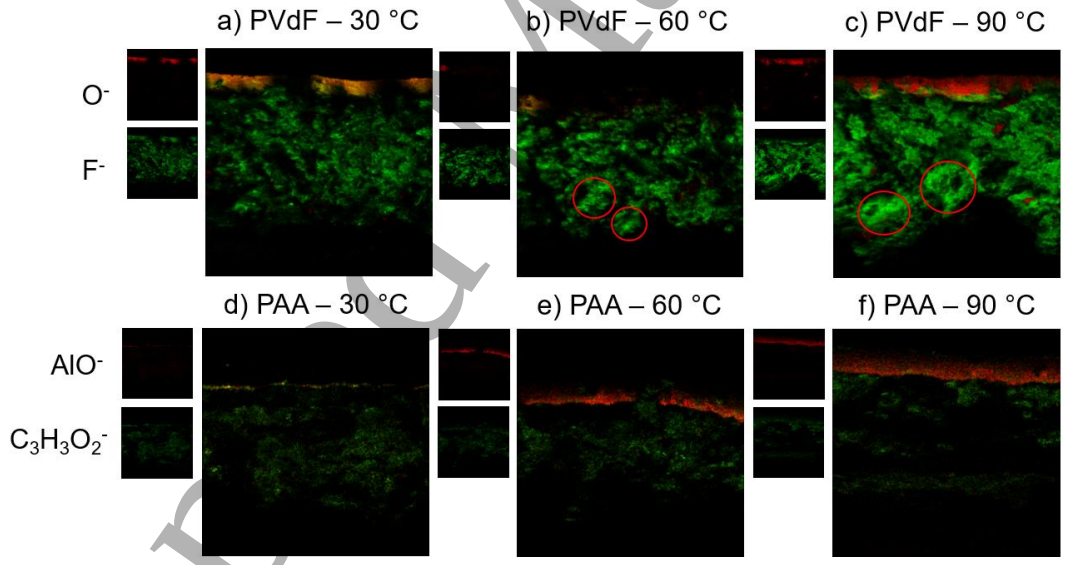

Figure 5: ToF-SIMS images of the electrode cross-sections with intensity scales matched to enable for comparison within the binder type. Upper panel: pristine PVdF-based electrode coatings dried at 30 °C (a), 60 °C (b) and 90 °C (c) with F^- (green) as the detected binder fragment. Lower panel: pristine PAA-based electrode coatings dried at 30 °C (d), 60 °C (e) and 90 °C (f) with $C_3H_3O_2^-$ (green) as the detected binder fragment. The current collector (C coated on Al) is on top of the images and detected based on the O^- (red) or AlO^- (red) fragment. The raster scanning area is 150 x 150 μm^2.